PAPER

Check for updates

From molecular to nanoplastic SERS detection: insights into the role of analytes in plasmonic substrate design

Ioana Cârdan, [a,b] Veronica Zani, [c] Ana Maria Mihaela Gherman, [a] Raffaella Signorini, [c] Roberto Pilot (ID) [c] and Cosmin Farcău (ID) *[a]

Nanoplastics are nowadays a significant subject of interest due to their potential negative impact on human health and environmental quality. Their submicron size necessitates innovative analytical techniques like surface-enhanced Raman scattering (SERS), which proves highly effective in trace molecular detection within the nanometer range. Although SERS technology has advanced significantly, there is a largely unexplored gap between demonstrating the efficiency of SERS substrates with probe molecules and the practical use of these substrates for nanoplastic detection. Therefore, this study explores whether the optimization of a specific SERS substrate towards molecular analytes is also valid for the detection of individual nanoplastics. Since SERS relies on materials with nanoscale features, here we present a new class of nanostructured SERS substrates with different surface morphologies and tuned plasmonic response fabricated by the colloidal lithography technique. In this regard, we first performed the SERS enhancement characterization of the plasmonic substrates functionalized with a molecular analyte (benzenethiol) by wavelength-scanned surface-enhanced Raman scattering measurements in the near-infra-red spectral range. Furthermore, we investigated the SERS performance of the substrates for the detection of individual polystyrene spherical nanoplastic particles and the experimental results were corroborated with finite-difference time-domain (FDTD) analysis. The results indicate that while a SERS substrate optimized for molecular analytes may show excellent efficiency, separate optimization is necessary for efficient detection of individual nanoplastic particles.

1. Introduction

The mismanagement of plastic waste disposal[1] results in increased release and accumulation of substantial quantities of plastic litter in the natural environment.[2] The debris first undergoes deterioration which subsequently results in its fragmentation[3] into smaller particles, referred to as secondary microplastics and nanoplastics. According to the International Organization for Standardization (ISO/TR 21960:2020),[4] microplastics are defined as plastic particles with a size limit of 1 μm, while nanoplastics are particles with a size smaller than 1 μm. The occurrence of microplastics is highly reported at different levels in the environment, from aquatic organisms,[5] including fishmeal[6,7] to human blood[8] or even in human placenta.[9] Moreover, their presence has also been confirmed in the terrestrial environment,[10] atmosphere,[11] and aquatic

environments,[12] such as spring water,[13] freshwater,[14] and even in drinking water.[15] Even though nanoplastics are considered potentially more toxic than microplastics due to their larger specific surface area,[16] studies related to the occurrence, fate and impact of nanoplastics are scarcely found or are incomplete.[17] The main factor contributing to this lack of studies is that the detection and identification methods commonly used for microplastics are ineffective for nanoscale plastic particles. As the size of particles decreases, it becomes increasingly challenging to detect them in the environment, therefore being categorized as an invisible threat to both the environment and the biodiversity of our planet. Currently, the most frequently employed techniques for chemical identification of microplastics are mass spectrometry-based methods[18] and vibrational spectroscopies,[19] such as Fourier-transform infrared spectroscopy (FTIR)[20] and Raman micro-spectroscopy.[21] Among these, FTIR and Raman spectroscopy methods are the most widely applied for microplastic analysis,[19] as they are powerful analytical tools for identifying synthetic polymers with diverse chemical structures, compositions, and potential additive content.[22] However, due to the limited sensitivity of these two analytical methods, the detection of sub-micrometer plastic

[a] National Institute for Research and Development of Isotopic and Molecular Technologies, Cluj-Napoca, Romania. E-mail: cfarcau@itim-cj.ro
[b] Faculty of Physics, Babeş-Bolyai University, Cluj-Napoca, Romania
[c] Department of Chemical Sciences and INSTM Research Unit, University of Padova, Padova, Italy

particles is rather difficult and challenging. Consequently, the number of studies that have focused on the detection of nanoplastics is still very small.[23] However, significant efforts have been made to overcome the inherently low sensitivity of Raman spectroscopy, leading to the development and use of advanced Raman-based methods such as surface-enhanced Raman scattering (SERS), resonance Raman spectroscopy (RRS), and tip-enhanced Raman Spectroscopy (TERS), among others.[24,25] Among these, the SERS technique[26–28] is one of the most sensitive, facile and highly available methods in laboratories for obtaining chemical information of sub-micrometer particles and in low concentrations. The performance of SERS technology relies on the enhancement of Raman scattering signals from the analyte, achieved through the use of plasmonic nanostructured surfaces, commonly referred to as SERS substrates.[29] The nanoscale surface features of the SERS substrates play a key role in enhancing the Raman scattering of analytes through electromagnetic field enhancement effects induced by surface plasmon resonances. However, despite its acknowledged benefits and numerous SERS substrates developed for the analyses of molecular analytes, to date, a relatively limited number of studies have successfully detected nanoplastics by using the SERS method.[30] In the available existing literature, the detection of nanoplastics with SERS is reported by using both colloidal suspensions of metal nanoparticles[31–36] and nanofabricated plasmonic solid substrates,[37–42] including commercially available ones.[43] While metal colloidal suspensions are commonly used as SERS substrates, solid SERS substrates exhibit superior characteristics that are more desirable from a practical perspective. These features include uniformity, reproducibility, a large surface area, stability, low cost, and high enhancement.[44] However, it is still challenging to have all these features at once by using the conventional advanced lithographic techniques. An alternative to these advanced lithographic techniques is the colloidal lithography (CL) technique,[45] which is known to be rather simple, low-cost, and highly efficient and feasible for more laboratories, offering good-enough reproducibility and good control over the fabricated area. CL involves the use of self-assembly strategies for the formation of colloidal crystals with specific patterns and optical properties. By depositing metal films over colloidal crystals, plasmonic nanostructured substrates are obtained, which can be used for optical sensing,[46] including SERS substrates.[47]

It is well known that the performance of nanostructured solid SERS substrates is strongly dependent on the structural arrangement and geometry of the nano-micro-scale features of the surface. This is because shape and size dictate the surface plasmon resonances, which in turn produce the electric fields responsible for SERS enhancements. Besides, the enhancement can originate from features on the nm-scale, *i.e.* SERS 'hotspots',[48] which cannot be reproduced or characterized with great confidence. In typical SERS experiments, analyte molecules adsorb onto the metal surfaces and ideally can cover the whole SERS substrate, reaching the sites of high field enhancement. On the other hand, when considering SERS from nanoplastics, there will be a limited contact area between the plastic particle and the SERS substrate. Depending on the plastic's shape and size, this area of contact could be or not a region of high field enhancement. Therefore, one important question to ask is whether the optimization of a certain SERS substrate towards molecular analytes makes it a good SERS substrate for nanoplastics. Another important aspect to mention is that the majority of the SERS studies cited above[37,38,42] have analyzed agglomerations of nanoplastics, such as coffee rings.[49] However, the ability to detect and analyze individual nanoplastics would open up more perspectives and more precise analytical protocols for real-life samples where mixtures of particles of different chemical compositions exist.

This study aims to determine if knowledge gained from molecular SERS studies on plasmonic nanostructured substrates can also be applied to individual nanoplastics. One important question is whether the optimization of a specific SERS substrate towards molecular analytes is also valid when this SERS substrate is used for the detection of individual nanoplastics. We first prepared two nanostructured SERS substrates with different surface morphologies and tuned plasmonic response. These were fabricated by combining colloidal self-assembly, (optional) plasma etching, and metal coating by physical vapor deposition. We evaluated the performance of these customized SERS substrates using wavelength-scanned SERS with a known molecular Raman reporter (benzenethiol) in the near-infrared (NIR) spectral range. Considering the results obtained for the molecular analyte, we further investigated the substrates' efficiency in detecting individual nanoparticles such as polystyrene spherical nanoplastic particles (SNP) with diameters of 300 nm and 500 nm. The experimental results were corroborated with FDTD analysis giving more insights into detecting individual nanoplastic particles with nanostructured SERS substrates. An intriguing finding was that, although one type of SERS substrate was optimized for SERS on molecular analytes, the other type was more efficient for nanoplastic detection. Therefore, a separate, specific optimization of the SERS substrates is required for nanoplastic detection, taking into account also the morphological and geometrical constraints.

2. Materials and methods

2.1. Materials/chemicals and reagents

Benzenethiol (BT) (purum, 98% GC) was purchased from Fluka. Polystyrene (PS) nanoparticles with diameters of 300 nm (10% (w/w) in water), 460 nm (10% (w/w) in water) and 500 nm (2% (w/w) in water) were purchased from Sigma-Aldrich Co. Ultrapure water obtained with a Milli-Q® direct water purification system was used throughout all experiments. Ethanol, methanol and isopropyl alcohol were purchased from Merck KGaA, Darmstadt, Germany.

2.2. SERS substrate fabrication

Two variants of SERS substrates were fabricated by means of colloidal lithography, as schematized in Fig. 1. Air–water inter-
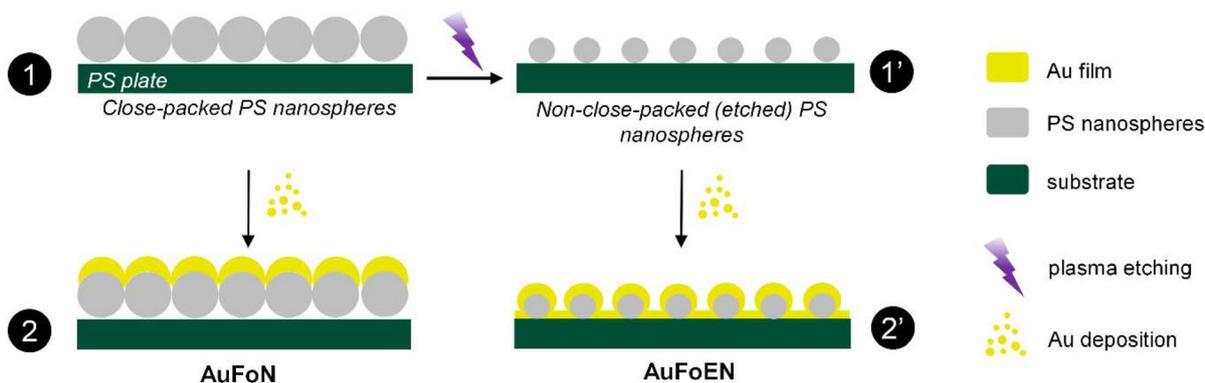
Fig. 1 The schematic representation of the fabrication process of the two SERS substrates, AuFoN and AuFoEN, respectively.

facial self-assembly was the first step applied in the fabrication process of the substrates, involving the assembly of 460 nm PS spheres into highly ordered, close-packed 2D arrays over a 2 × 4 cm² PS plate (Fig. 1, step 1). Before starting the self-assembly procedure, the PS spheres and the PS plates were subjected to a cleaning procedure. Fifty µL of PS suspension was mixed with 50 µL of deionized water and 100 µL of ethanol and the resulting solution was centrifuged at 7000 rpm for 10 min using a Bioprocen 22 R centrifuge (Ortoalresa, Madrid, Spain). After centrifugation, the supernatant was removed, and the precipitate was redispersed in 80 µL of deionized water and 100 µL of ethanol. The resulting PS solution was ultrasonicated for 3 min. The PS plates were cleaned following three steps. At first, the plates were immersed in methyl alcohol and then isopropyl alcohol, followed by blow drying with N₂ gas, and finally, the plates were exposed to a UV–ozone (Ossila Ltd, Sheffield, UK) cleaning procedure for 20 minutes. The equipment used in assembling the PS spheres consists of a laboratory syringe pump equipment, Ossila double syringe pump (Ossila Ltd, Sheffield, UK), which allows an automatic dispensing of PS suspension onto the liquid surface. Prior to deposition, the PS plates were placed on a 5 degrees tilted support which was further positioned in a Petri dish, and 50 mL of ultrapure water was then poured into the Petri dish. As this step was completed, a small volume of PS suspension (~70–80 µL) was withdrawn into the capillary tube (with a diameter of 2 mm) which was connected to a 12 mL syringe and motorized by the syringe pump equipment. Coming through the capillary tube in contact with the water, the PS spheres were spread on the liquid surface at a constant rate of 0.398 µL s⁻¹ until the liquid surface was completely covered with spheres. The 2D nanostructures self-assembled on the liquid surface were then easily transferred onto the PS plates by withdrawing the water from the Petri dish by another capillary tube connected to a syringe which was also controlled by the Ossila syringe pump equipment. As a final step, the ordered arrays of PS spheres obtained over the substrate were simply left on the angled supports until they were completely dried. The deposition was made under ambient conditions. The next step con-

sisted of etching for 270 s a few samples of the ordered arrays of PS spheres under air-plasma (60 W, 0.7 mbar) resulting in a non-close-packed pattern (Fig. 1, step 1′). The plasma etching treatment was made using a low-pressure FEMTO plasma system (Diener Electronic GmbH⁺ Co. KG, Germany). In the final step, both the close-packed and the non-close-packed (etched) sphere arrays were coated with a 150 nm thick gold film by electron-beam evaporation, employing the Kenosistec KE 400E (Kenosistec, Italy) equipment. Thus, as illustrated in Fig. 1, step 2 and 2′, we fabricated two distinct types of SERS substrates: gold film over nanospheres (AuFoN) and gold film over etched nanospheres (AuFoEN).

2.3. Morphological and optical characterization

The surface morphology of the prepared SERS substrates was analyzed by scanning-electron microscopy (SEM) measurements using a Hitachi SU8230 system. SEM images were used not only to observe the substrate's morphology, but also to estimate various parameters, such as sphere diameter and interparticle distance using ImageJ software. SEM analysis was also performed on the SERS substrates drop-coated with PS SNP to examine the placement of the SNPs on the substrates. The optical properties of the SERS substrates were determined with a uSight-2100 system (Technospex, Singapore) which consists of a vis-NIR spectroscopy module integrated into a Nikon upright microscope. We collected the specular reflection within the spectral range of 400–1000 nm using a 4× magnification objective lens (N.A. 0.13, W.D. 17.2) and a broadband dielectric mirror (Thorlabs) as a reference.

2.4. Wavelength-scanned SERS measurements on molecules

Raman measurements were performed using a custom-built Micro-Raman setup. Excitation was provided by a continuous-wave titanium-sapphire laser (Spectra Physics 3900S), tunable within the near-infrared range of 675–1000 nm and pumped by a semiconductor laser (Coherent, Verdi G7) at 530 nm. The laser beam was directed into an Olympus BX 41 microscope and focused onto the sample using a 20× objective (Olympus LMPlan FLN 20×, NA = 0.40). The Raman scattering was col-

lected in back scattering configuration, coupled into the slit of a three-stage subtractive spectrograph (Jobin Yvon S3000) and detected using a liquid nitrogen-cooled CCD (Jobin Yvon, Symphony, 1024 × 256 pixels, front illuminated). The three-stage spectrograph comprises a double monochromator in subtractive configuration (DHR 320) paired with a single spectrograph (HR 640). The former acts as a tunable notch filter and allows rejection of Rayleigh scattering at the desired wavelength.

For the SERS characterization, BT was used as a Raman reporter. Thus, the substrates were functionalized by immersion in 10 mM BT solution in ethanol overnight. After incubation, the functionalized substrates were washed with the solvent and left under ambient conditions until their complete drying. The SERS measurements were performed with laser excitation in the range of 710–850 nm, using an interval of 10 nm. Both substrates were scanned at each wavelength collecting 10 different spectra from random positions on the substrate. Each spectrum was collected between 900 and 1190 cm^{-1} with 10 acquisitions, 10 s integration time, and a laser power of 0.13–0.28 mW. The Raman spectrum of liquid BT was also measured at each wavelength under the same conditions as described above.

2.5. SERS enhancement factor estimation

For the estimation of the SERS enhancement factors, the following formula was used:[50]

$$EF = \frac{I^{SERS}}{I^{Raman}} \cdot \frac{C_v}{C_s} \cdot \frac{\eta}{A}, \tag{1}$$

where I^{SERS} was estimated by integrating the intensity of the 999 cm^{-1} band of the BT molecules adsorbed on the SERS substrates and I^{Raman} by integrating the intensity of the same band of liquid BT. C_v is the number of molecules per unit volume of liquid BT and is equal to 5.88×10^{21} molecules per cm^3. It was calculated by using the relation, $C_v = \frac{dN_A}{W_m}$, where d is the density of liquid BT (1.077 g cm^{-3}), W_m is the molecular weight and is equal to 100.19 g mol^{-1} and N_A is the Avogadro number. C_s is the surface packaging density of BT and from the literature it was considered to be equal to 6.80×10^{14} molecules per cm^2.[51] η is the collection efficiency of the equipment used, and it was determined by collecting the Raman signal of the reference (silicon) at different positions along the z optical axis, using a regular distance interval of 5 μm. The intensity of the silicon 520 cm^{-1} band, as a function of sample position, was fitted with a Voigt profile. The full width at half maximum (FWHM) of the fit was then used as the estimate for η. This procedure was followed at each laser wavelength, and η had values in the range 28–122 μm. A is known as the geometrical factor and is defined as the ratio between the exposed surface and the area of the unit cell. We made use of the SEM images for the calculation of A, and the values estimated by taking into account both the semi-spherical metal coating on top of the spheres and the metal coating on the substrate below the spheres are 1.87 for AuFoN and 1.32 for AuFoEN.

2.6. SERS measurements of nanoplastics

At first, homogeneous dispersions of polystyrene SNPs with diameters of 300 nm and 500 nm were used for nanoplastic detection. The work suspensions of PS SNPs were cleaned using the following procedure: 50 μL of PS suspension were mixed with 50 μL of ethanol; the resulting mix was centrifuged at 9000 rpm for 15 min and 4500 rpm for 10 min, for the 300 nm and 500 nm suspensions, respectively; after centrifugation, the supernatant was removed and the precipitate was redispersed in 100 μL of ethanol following a second washing procedure under the same conditions; the precipitate resulting this time was redispersed in 50 μL of ethanol and the suspension obtained was further diluted 100 times. Prior to deposition, the AuFoN and AuFoEN substrates were exposed for 20 minutes to a UV–ozone cleaning procedure to increase their hydrophilicity and further ensure a good dispersion of the PS SNPs on the substrates. From each of the two prepared PS SNP dispersions, a volume of 5 μL was drop coated on the two SERS substrates and on a cover glass for reference. As a cleaning procedure before deposition, the cover glass was immersed in acetone, methyl alcohol and isopropyl alcohol and then dried under a N$_2$ gas flow. As the PS nanoplastic particles were deposited on AuFoN, AuFoEN and on cover glass, we performed the SERS measurements with 785 nm (120 mW) excitation line using a Renishaw InVia Reflex confocal Raman system (Renishaw, Wotton-under-Edge, Gloucestershire, UK). All spectra were collected in the fingerprint region of polystyrene (800–1600 cm^{-1}) and with a 100× (NA 0.9, WD 3.4 mm) objective lens as the spectra were collected from individual PS SNPs. Ten seconds of exposure time, 1 accumulation and a power of 1 mW were used for the acquisition of each spectrum. The processing of the spectra consists in baseline subtraction/corrections.

2.7. FDTD electromagnetic simulations

The electromagnetic near-fields on a hexagonal structure of gold film over nanospheres were studied using the finite-difference time-domain (FDTD) method implemented in Ansys Lumerical software. Two arrangements are considered, corresponding to the AuFoN and AuFoEN systems and, for each of them, the electric field enhancement was analyzed with and without a spherical polystyrene nanoplastic positioned on top. Spherical nanoplastics of 100 nm, 300 nm, and 500 nm in diameter were investigated. Both structures are based on a monolayer of 86 PS spheres covered with a gold film which is represented as a spheroid cap and has a thickness of 50 or 150 nm. These are placed on a SiO$_2$ substrate. For the AuFoN structure, the spheres have a diameter of 460 nm and are tightly packed (Fig. S1a), while for the AuFoEN (Fig. S1b), the spheres' diameter is 300 nm, and the interparticle centre-to-centre distances are still 460 nm. The parameters applied for defining the gold spheroids are detailed in the paper by Nechita *et al.*[52] Both arrangements are irradiated with a Gaussian beam that is focused on the center of the polystyrene nanoplastic, propagates in the $-z$ direction and is polarized in

the x direction. For this study, we assumed that the beam waist diameter has the same order of magnitude as the laser wavelength, thus the thin lens setting is used, assuming a numeric aperture of 0.9. Moreover, the study was carried out for 785 nm excitation wavelength. It is assumed that the system is symmetric in the x direction and that, at the boundaries, there is a perfectly matched layer. For 100 nm above and below the plasmonic structure, but also for the nanoplastic sphere on top of the metal film, a mesh with a spatial resolution of 4.6 nm was used. Instead, for the SiO_2 substrate and in the air away from the metal-coated spheres a mesh accuracy factor of 6 was used and a conformal variant 1 mesh refinement. The mean electric field (Mean E) in the AuFoN and AuFoEN structures was computed over an area comprising 7 neighboring gold coated nanospheres that represent a periodic unit of our system. Thus, Mean E was computed at the surface of the gold thin film, 5 nm above the gold surface to avoid any singular points (Fig. S1 in the SI). For the polystyrene SNP situated on glass, AuFoN and AuFoEN, we determined the mean electric field by averaging over the whole volume of the particle.

3.   Results and discussion

3.1.   Morphological and optical characterization

SERS substrates with different morphologies were obtained following the simple fabrication procedure based on the colloidal lithography technique illustrated in Fig. 1. The monolayer colloidal arrays of polystyrene spheres obtained by means of air–water ISA method (Fig. 1, step 1) present a uniform and close-packed hexagonal arrangement[53] as can be observed in the SEM image of the AuFoN in Fig. 2a. Alternatively, by exposing these close-packed arrays to an air-plasma procedure for 270 s before the gold coating, we produced a non-close-packed monolayer of polystyrene spheres coated in gold (AuFoEN), as shown in Fig. 2b. Therefore, the etching process allowed us to produce two different metal film morphologies and then investigate how these morphologies impact detection capability. The morphology-induced changes during the etching procedure were investigated by electron microscopy and the

results clearly show a reduction of the particle size and an enlargement of the interparticle distance with etching. According to SEM images, we determined that the unetched polystyrene spheres have an average diameter of 422 nm ± 7.8 nm, instead of 460 nm as indicated by the product specifications, probably due to compression forces exerted between the spheres during the self-assembly process, and/or imprecise specifications. Next, applying the etching procedure for 270 s, the average diameter of the spheres was reduced to 263 nm ± 7 nm, while introducing an average interparticle spacing of 168 nm ± 32 nm. Besides these modifications, when etching the spheres, we also noticed a change in their sphericity, which results in a slight increase of their surface roughness. However, the use of a relatively thick gold film hides and smooths the surface roughness of the etched spheres.

We further examined the optical response of the metal-coated spheres as a function of the etching process, and thus the morphology. Fig. 2c shows the experimental vis-NIR reflectance spectra of the two SERS substrates, AuFoN and AuFoEN, respectively. The SERS substrates have the photonic response between 500 nm and 950 nm, and it can be seen how each spectrum is characterized by distinct features being correlated with the morphology previously changed through the etching procedure. The reflectance spectrum of the unetched substrate, AuFoN, is dominated by a broad dip at 765 nm in the infrared range, while the AuFoEN substrate exhibits a similar dip at 721 nm (dips indicated by the arrows in Fig. 2b). The reflectance dip characteristic of the AuFoEN substrate is blue-shifted by 44 nm and is narrower than the dip characteristic of AuFoN. The reflectance minima observed for AuFoN substrates are known to be associated with excitation of localized surface plasmons, manifested through near-field enhanced fields that occur between adjacent metal half-shells.[52]

The changes in the sphere diameter and in the interparticle distance induced through etching, influence the plasmonic response of the AuFoEN, as already shown in Fig. 2c. Understanding in depth the nature of the plasmonic response of the AuFoEN structure is beyond the scope of the current study, and will be the subject of future work, together with the evolution of the plasmonic response determined by various etching times. As also known from previous studies, the reflectance dips indicate the spectral range of good SERS activity for this kind of SERS substrates. Based on their reflectance spectra, both the AuFoN and the AuFoEN are expected to perform as efficient SERS substrates in the 600–900 nm range. Therefore, even though the two types of SERS substrates fabricated exhibit different morphologies, they both offer good SERS activity in the spectral range tested.

3.2.   SERS enhancement characterization with a molecular analyte

The SERS enhancement characterization of the two substrates was performed by means of wavelength-scanned SERS spectroscopy measurements. The SERS enhancement profile was determined by scanning the excitation laser wavelength with an increment of 10 nm, in the spectral range between 710 nm
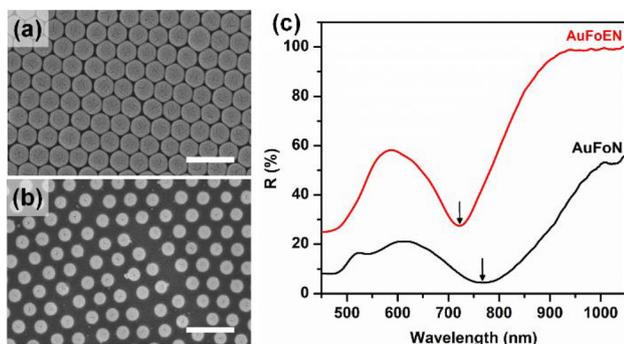

Fig. 2 SEM images of (a) AuFoN and (b) AuFoEN substrates, and (c) their corresponding reflectance spectra. Scale-bar in (a) and (b) is 1 μm.
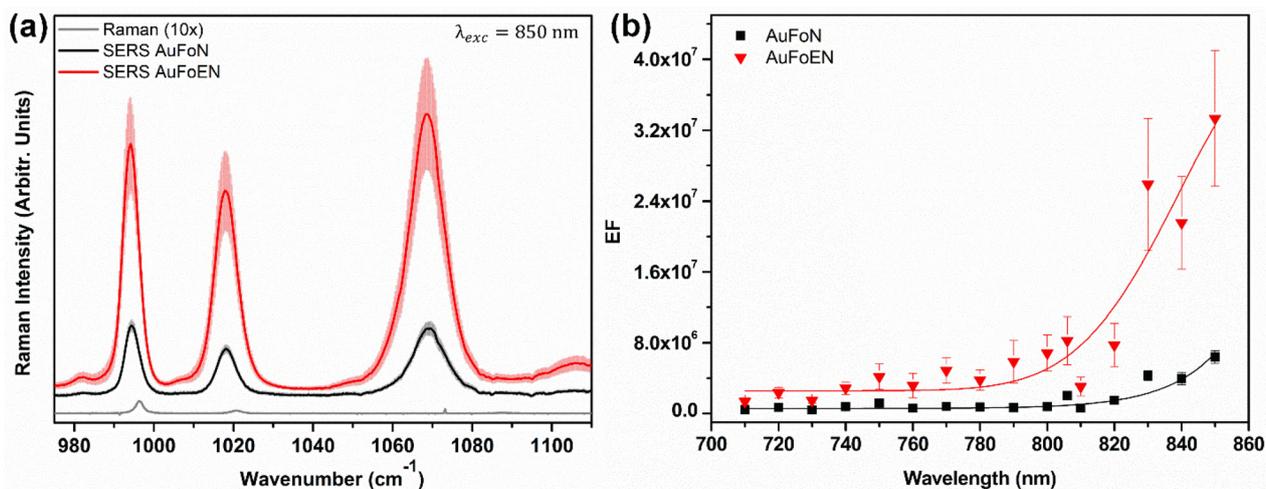
Fig. 3 (a) The Raman and SERS spectra of BT molecules under excitation at 850 nm, including standard deviation (SD); (b) the SERS enhancement profile of the two SERS substrates in the range of 710–850 nm; lines serve as guide for the eye.

and 850 nm. Fig. 3a shows the Raman spectrum of BT and the SERS spectra of BT functionalized AuFoN and AuFoEN, excited at 850 nm, including standard deviation (SD) obtained from repeated measurements. The characteristic signals of BT were observed for both substrates, with strong Raman bands at 993 cm^{-1} (β_{CCC}), 1018 cm^{-1} (β_{CH}), and 1068 cm^{-1} (β_{CH}), with their assigned modes in parentheses, where β and ν represent the in-plane bending and the stretching modes, respectively.[54] The peak positions of BT in the SERS spectra are shifted to a lower energy relative to those in the Raman spectrum, due to the interaction between the BT molecules and the gold surface; molecules are bound to the gold surface, and thus their vibrations are modified.

The enhancement factor at each wavelength was calculated as described in the Experimental section, and we subsequently obtained the SERS enhancement profile displayed in Fig. 3b. For both substrates an increase of the EF with wavelength is observed, obtaining the best enhancement in the NIR range (830–850 nm). It is worth mentioning that the SERS enhancement is not well correlated to the plasmonic response as indicated by the reflectance spectrum. We note that a red-shift is observed for the EF maximum (Fig. 3b) relative to the reflectance minimum (Fig. 2c) for both substrates and assume that the enhancement factor reaches its maximum above 850 nm. Such a behaviour has been already reported for plasmonic nanostructures and has been explained by Zuloaga and Nordlander.[55] Using a simple analytical harmonic oscillator model, the authors showed that the shift is directly related to the total damping in the system. In our case, the relatively large morphological features of the substrates also resulted from the smooth and continuous gold film produced by electron-beam evaporation,[56] leading to increased radiative damping, which in turn causes the observed spectral shifts. The EF goes up to 6.3 × 10^6 for the AuFoN and 3.3 × 10^7 for the AuFoEN. Therefore, the best enhancement was obtained for

AuFoEN substrate, suggesting that the different features at the micro-nano scale of the substrate influenced its SERS performance. Besides the different distribution of electromagnetic near-fields, and a possibly different balance between absorption and scattering (to be further investigated), the enhanced SERS performance of the AuFoEN substrate can be also attributed to its slightly higher rugosity (Fig. 2b) leading to more confined SERS hot spots. However, a higher enhancement of a SERS substrate can lead to lower uniformity/reproducibility.[57] This phenomenon is illustrated in Fig. 3a, where the reproducibility over the AuFoEN substrate surface is slightly lower than for the AuFoN substrate, which exhibited a lower enhancement. Specifically, the standard deviation of the signal with respect to the average intensity of the band at 1068 cm^{-1} is 8% for AuFoN and 20% for AuFoEN, resulting in a ratio of 2.34 that highlights the difference in reproducibility over the two substrates.

3.3. SERS of single-particle polystyrene nanoplastic

In the previous section we determined that SERS performance of the substrates is related to structure at the micro-nano scale, obtaining the highest EF for the AuFoEN substrate. However, here we aim to determine if the optimization of the SERS substrates towards molecular analytes (BT in our case) is also valid for nanoplastic particles. In order to determine if the SERS substrates possessing larger EF, as measured with the BT molecular analyte, perform better also in the case of nanoplastics, we next tested both AuFoN and AuFoEN in the detection of PS SNPs. We chose to focus on 500 nm sized particles, as they are slightly below the limit where standard Raman spectroscopy is effective; individual 1 μm particles can be detected by Raman micro-spectroscopy without much difficulty, but 500 nm ones start to be problematic, due to their size. We added 300 nm particles in the study to move towards even lower particle sizes. The PS SNP suspensions

with diameters of 300 nm and 500 nm were dispersed on both substrates, and the analyses were performed with the 785 nm excitation line, since this corresponds to a common laser type. We achieved the desired dispersion of SNPs over the substrates, as is evidenced in Fig. 4a and b where we observe the same area under dark-field and bright-field conditions, respectively. These images highlight a region at the edge of the deposited and dried droplet, where a coffee-ring was formed. Many dispersed individual SNPs (indicated in circles) are visible in the area inside the ring, while the upper-right corner lying outside of the coffee-ring is free of SNPs, as clearly seen especially in the dark field image. The SERS measurements were performed by focusing the laser on individual nanoparticles, under the microscope (with 100× magnification). The criterion for localizing a single SNP was based on its regular and spherical shape, as is highlighted in the inset image of Fig. 4b. The SERS results obtained with AuFoN and AuFoEN substrates are presented in Fig. 4c and d, respectively. In Fig. 4c, the displayed SERS spectrum represents the average of four individual SERS spectra collected from SNPs at different positions on the AuFoN substrate, with the individual spectra shown in Fig. S2. For AuFoN we observed a highly enhanced characteristic Raman signal of PS compared with the signal detected for the SNP on a plain glass substrate. The signal of the PS SNPs is distinctly noticeable, as evidenced by two prominent bands at 1003 cm^{-1} and 1033 cm^{-1} corresponding to the ring breathing mode of C–C and in-plane

deformation of C–H.[58,59] It is evident that the signal varies based on the SNP dimension, with a higher signal observed for 500 nm SNPs (Fig. 4c). However, when it comes to obtaining the SERS signal with the AuFoEN substrate, we encountered some challenges. Compared to the AuFoN substrate, we barely could obtain a signal from the AuFoEN substrate (Fig. 4d), contrary to the expectations derived from our molecular analyte SERS studies in Section 3.2.

To get more information which could help in understanding these results, we examined also SEM images of SNPs (marked with purple circles) deposited on top of AuFoN and AuFoEN, as presented in Fig. 4e and f, respectively. The exact placement of the SNPs on the substrates can be observed. In case of both substrates, the SNPs are located in the areas of lowest potential energy, typically at the center of a triangle formed of three adjacent spheres. This placement allows the spheres to take advantage of a specific sensing area, and interact in a specific way with the more or less enhanced fields in that region. Therefore, considering the SERS results, we can suggest that the existing space between gold half-shells of the AuFoN substrate is more favorable for SNPs to benefit from the sensing area compared to that of the AuFoEN. To conclude this section, the enhancement of signal intensity appears to be strongly influenced by the morphology of the substrate and how the nanoplastic particles fit onto its surface topology. Moreover, the particle size is also important as seen in the SERS results in Fig. 4c where a different enhancement was
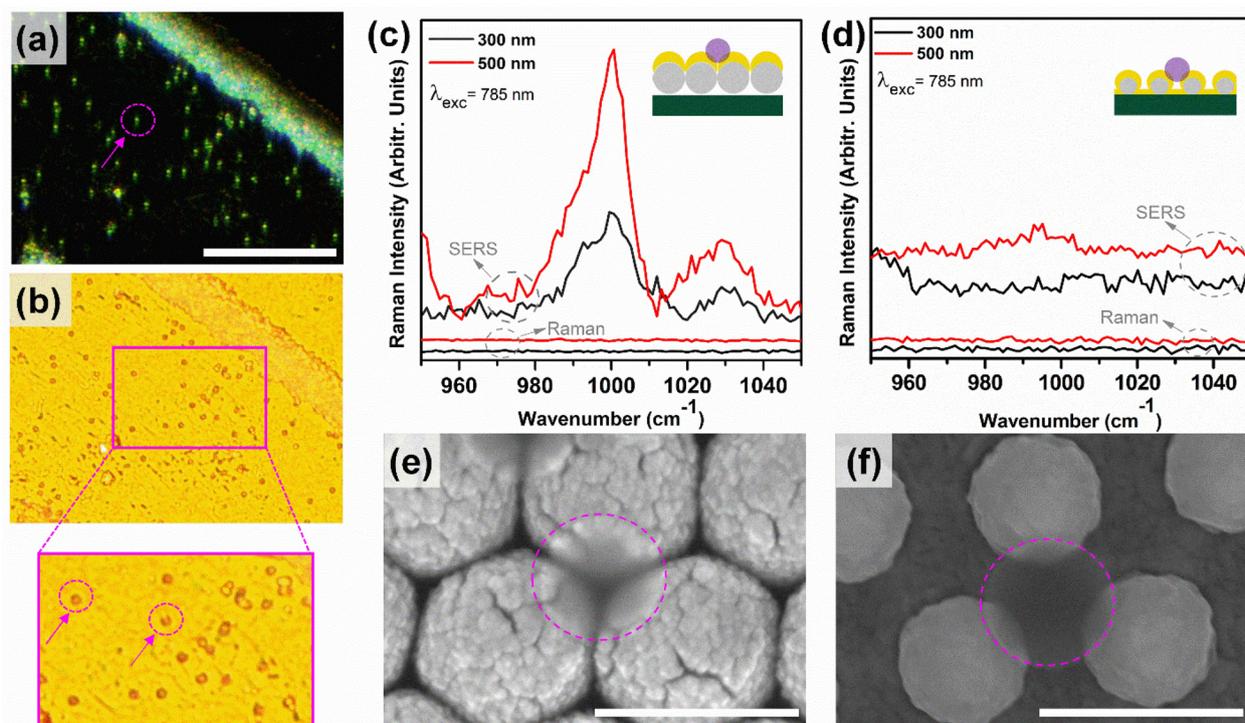

Fig. 4 (a) Dark field and (b) bright field images of the same area on the AuFoN substrate illustrating the 500 nm PS SNPs spread near the coffee-ring; (c) and (d) average SERS spectra of individual SNPs of 300 nm and 500 nm spread on AuFoN, and on AuFoEN substrates, respectively (785 nm excitation), together with Raman spectra of 300 nm and 500 nm SNPs on cover glass; (e) and (f) SEM images of 300 nm PS SNPs dispersed on AuFoN and AuFoEN substrates, respectively. Scale bar is 20 μm in (a and b) and 400 nm in (e and f).

obtained for the two dimensions of the SNPs, these results being consistent with the literature.[43] These dependencies should be taken into consideration in future studies aimed at developing and optimizing SERS substrates for nanoplastic detection.

3.4. FDTD analysis of single-particle SERS enhancement

As already mentioned, in typical SERS experiments, molecules adsorb to the metal surfaces and usually can access the whole surface of the SERS substrate, thus reaching the sites of highest field enhancement. This region of high field enhancement is typically located at the surface, with electric field intensities decaying few nanometers away from the metal surface (the region highlighted in purple on the left of Fig. 5). On the other hand, when considering SERS from nanoplastics, there is a limited contact area between the plastic particle and the SERS substrate. The region where high field enhancements are needed is located within the plastic particle (the spherical region highlighted in purple on the right of Fig. 5).

To inquire about the electric field enhancement inside the SNPs, full three-dimensional FDTD simulations of PS particles positioned on top of various substrates were performed. Fig. 6a presents the electric field magnitude at the 785 nm excitation wavelength, in a cross section through the 300 nm (top) and 500 nm (middle) SNPs placed on top of a plain glass substrate (left), on an AuFoEN (middle), and on an AuFoN substrate (right).

A first, interesting observation that can be visually made, is that the enhanced electric fields inside the SNP appear to extend over a larger portion of the SNP for the AuFoN case, both for 300 nm and 500 nm SNPs. In Fig. 6b the electric field magnitude cross sections through the bare AuFoEN and AuFoN substrates are also shown, while the average field over the surface, Mean E, is presented at the bottom of Fig. 6c, suggesting that comparably high electric fields are generated near the metal surface in the case of the two bare gold films. For a more quantitative assessment, the mean electric field

inside the SNP was then evaluated by averaging over the whole SNP volume, results being presented on the top panel of Fig. 6c. It can be observed that the mean electric field inside the SNPs is greater for the SNPs placed on top of the AuFoN than for the one placed on the AuFoEN, irrespective of the SNP diameter. As expected, the lowest electric field is encountered in the SNP placed directly on the glass substrate. Then, concerning the dependence on the analyzed SNP diameter: for AuFoN, a slightly higher mean electric field value was obtained inside the 300 nm SNPs (15.7 V m^{-1}) than inside the 500 nm SNPs (10.4 V m^{-1}); for the AuFoEN case, the electric field inside the 300 nm SNPs (8.7 V m^{-1}) is slightly lower than inside the 500 nm SNPs (7.9 V m^{-1}). Although differences of these absolute values are not huge, they were converted to a single particle SERS enhancement factor, roughly estimated as the fourth power of the ratio between the mean electric field in the SNPs placed on the plasmonic structure and the mean electric field in the SNPs placed on the glass substrate (middle panel on Fig. 6c). When analyzing this SERS enhancement factor, differences between AuFoN and AuFoEN become more obvious: for the AuFoN, values of 197 and 22 were obtained for the 300 nm and the 500 nm SNPs, respectively; for the AuFoEN, values of 18 and 7 were obtained for the 300 nm and the 500 nm SNPs, respectively. These observations might be explained by the specific pattern of the electromagnetic near fields that are generated at the metallic surface by a specific excitation, and its relation to the SNP shape and dimension relative to the empty spaces available to physically accommodate the nanoplastic particle. As an example, smaller SNPs might better enter in the space between the spheroid gold caps, but this is not sufficient, since the enhanced electromagnetic fields might be maximized at a different spatial location.

To inquire more on the interplay between the SNP diameters and the different SERS substrate morphologies as modified by the gaps between the PS spheres (controlled by etching process), we have performed additional FDTD simulations to cover the following cases: different sized SNPs (100, 300, 500 nm) deposited on non-etched 460 nm PS spheres, 460-etched-to-400 nm, 460-etched-to-350 nm, and 460-etched-to-300 nm sized particles coated in gold films (50 and 150 nm thick), and plain glass substrate as the reference. The mean electric field and estimated single particle SERS EF are presented in Fig. S3 of the SI. The most spectacular result concerns the smallest SNP, of diameter 100 nm, deposited on the AuFoEN substrate, for which the single particle SERS EF is much smaller than all other cases: due to the size, a 100 nm SNP falls in between the Au shells, and reaches the bottom region of the SERS substrate, thereby avoiding the highest electromagnetic field enhancement areas. Another interesting situation concerns the comparison between the two gold film thicknesses (50 and 150 nm) for 100 nm SNPs on the non-etched and on the 460-etched-to-400 nm geometries: while for the 50 nm thickness the maximum EF is reached by the AuFoN geometry, for the 150 nm thickness the maximum is reached by the AuFoEN geometry, due to the gold film thickness influencing both the plasmon field distribution of the
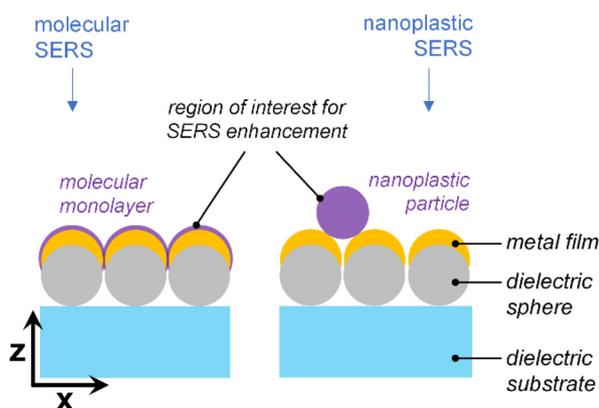

Fig. 5 Schematic representation of an AuFoN substrate, showing in purple the spatial regions where electromagnetic field enhancement is needed in the case of SERS on molecular analytes (left) and nanoplastic particles (right).
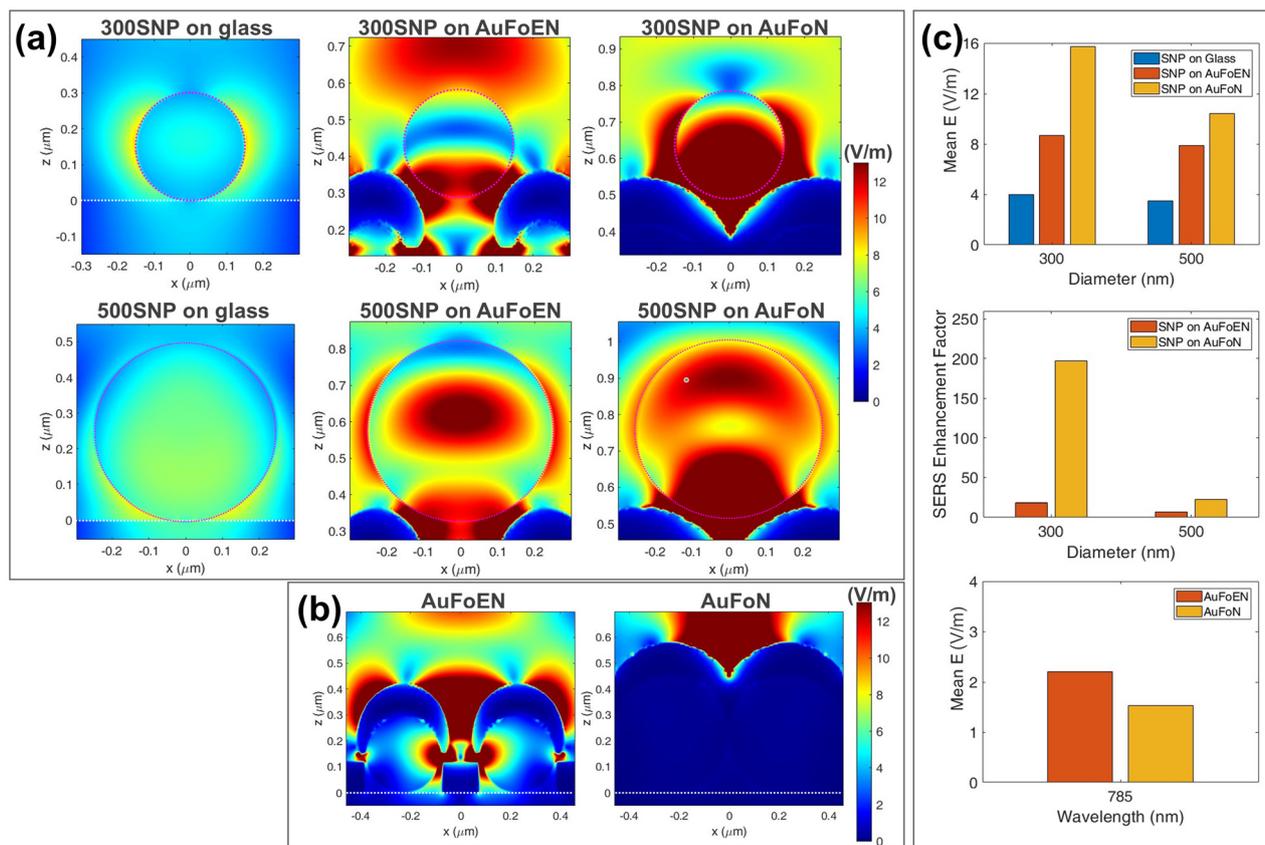
Fig. 6 (a) Electric field distribution at 785 nm inside the SNPs on a dielectric substrate, on AuFoEN and AuFoN (from left to right), for 300 nm (top) and 500 nm (middle) spheres; (b) electric field on the AuFoEN and AuFoN substrates; (c) mean electric field (top) and estimated SERS enhancement factor for the SNP (middle), and the mean electric field at the top of AuFoEN and AuFoN substrates (bottom).

nanostructured film and the final resting position of the SNPs. For 300 nm SNPs, the highest single particle EF is achieved for the AuFoN substrate and the least for etched AuFoEN. For SERS detection of 500 nm SNPs, the AuFoN substrate based on the thicker Au film provides the highest enhancement, while, interestingly the thinner Au film yielded almost constant EF for all analyzed systems. All these observations point to the crucial role of substrate geometry and the importance of physically matching the geometry of the SERS substrate to that of the analyzed nanoplastic. Finally, note that, even if for some cases the highest SERS EF was obtained for the 100 nm SNPs, this does not mean that the highest SERS signal collected in practice would be achieved from the 100 nm SNPs; the collected Raman signal is also proportional to the particle volume, which is almost an order of magnitude smaller for a 100 nm SNP than for a 300 nm SNP (see integral E field in Fig. S3).

Although these FDTD analyses are not expected to provide a full picture of the plasmonic/photonic interactions taking place in the real experiments, they can point to some important conclusions: (i) for the particular configuration in this study, the AuFoN substrate generated higher SERS enhancement factors than AuFoEN for detecting spherical nanoplastic particles, while the AuFoEN exhibits higher enhancement towards surface bound, small molecular analytes; (ii) more generally, there is a dependence of the amplification on the SNP diameter, which varies between the two SERS substrates analyzed, suggesting that one substrate may be more efficient for smaller SNPs, while the other could be better suited for larger SNPs.

4. Conclusions

One of the most interesting contributions of this work is towards the understanding of how plasmonic-based SERS amplification, whose effect has already been extensively studied on molecules and thin films, occurs on nanoplastic particles. To this end, two types of SERS substrates were fabricated using colloidal lithography. The first, termed gold film over nanospheres (AuFoN), was prepared by depositing a 150 nm gold layer onto a close-packed 2D array of polystyrene nanospheres. In contrast, the second substrate, gold film over etched nanospheres (AuFoEN), underwent an intermediate plasma etching step that reduced the nanosphere size while maintaining the interparticle center-to-center distance, thus

creating an array of gold coated spheres separated by gaps. The advantage of this approach was that it made available two SERS substrates exhibiting different morphological features, and it then enabled a direct comparison of the SERS detection performance between the two substrates across analytes of differing physical characteristics, namely benzenethiol (BT) molecules and polystyrene (PS) nanoplastic particles.

The SERS enhancement factor was measured using benzenethiol as a test molecule, by wavelength-scanned SERS: AuFoEN exhibited a larger enhancement than AuFoN across the whole 710–850 nm excitation range. In contrast, individual 300 nm and 500 nm plastic nanoparticles yielded a SERS signal when deposited on AuFoN, but not on AuFoEN: FDTD analysis supported this observation, demonstrating a larger amplification for both nanoplastic sizes on AuFoN compared to AuFoEN.

In this case study, we demonstrated that the SERS substrate possessing the largest enhancement, measured with a small molecular analyte, is not necessarily the most efficient one when hundreds of nm sized analytes, such as nanoplastics, are involved. A reasonable explanation is that small molecular analytes can penetrate into the extremely small spatial regions in which the electric field is localized (hotspots), whereas larger analytes may not. Consequently, the Raman signal amplification for these larger analytes will specifically depend on the interplay between their shape/size and substrate morphology. The previous considerations highlight that in designing SERS substrates for the detection of nanoplastics, it is necessary to consider not only the plasmonic response of the substrate itself but also its morphology and the analyte features, such as particle size and shape.

Conflicts of interest

There are no conflicts of interest to declare.

Data availability

Data for this article, including reflectance spectra and SERS spectra, are available on the Figshare repository at https://doi.org/10.6084/m9.figshare.29127098.

Supplementary information (SI) is available. See DOI: https://doi.org/10.1039/d5nr02181b.

Acknowledgements

References

1 M. G. Kibria, N. I. Masuk, R. Safayet, H. Q. Nguyen and M. Mourshed, *Int. J. Environ. Res.*, 2023, **17**, 1–37.

2 R. Geyer, J. R. Jambeck and K. L. Law, *Sci. Adv.*, 2017, **3**, e1700782, DOI: 10.1126/sciadv.1700782.

3 S. S. Ali, T. Elsamahy, E. Koutra, M. Kornaros, M. El-Sheekh, E. A. Abdelkarim, D. Zhu and J. Sun, *Sci. Total Environ.*, 2021, **771**, 144719.

4 ISO/TR 21960:2020 – Plastics—Environmental aspects—State of knowledge and methodologies, https://www.iso.org/standard/72300.html, (accessed 23 May 2025).

5 A. Alfaro-Núñez, D. Astorga, L. Cáceres-Farías, L. Bastidas, C. Soto Villegas, K. Macay and J. H. Christensen, *Sci. Rep.*, 2021, **11**, 1–8.

6 C. J. Thiele, M. D. Hudson, A. E. Russell, M. Saluveer and G. Sidaoui-Haddad, *Sci. Rep.*, 2021, **11**, 1–12.

7 J. Wu, M. Lai, Y. Zhang, J. Li, H. Zhou, R. Jiang and C. Zhang, *Case Stud. Chem. Environ. Eng.*, 2020, **2**, 100066.

8 H. A. Leslie, M. J. M. van Velzen, S. H. Brandsma, A. D. Vethaak, J. J. Garcia-Vallejo and M. H. Lamoree, *Environ. Int.*, 2022, **163**, 107199.

9 A. Ragusa, A. Svelato, C. Santacroce, P. Catalano, V. Notarstefano, O. Carnevali, F. Papa, M. C. A. Rongioletti, F. Baiocco, S. Draghi, E. D'Amore, D. Rinaldo, M. Matta and E. Giorgini, *Environ. Int.*, 2021, **146**, 106274.

10 C. Campanale, S. Galafassi, I. Savino, C. Massarelli, V. Ancona, P. Volta and V. F. Uricchio, *Sci. Total Environ.*, 2022, **805**, 150431.

11 I. Goßmann, D. Herzke, A. Held, J. Schulz, V. Nikiforov, C. Georgi, N. Evangeliou, S. Eckhardt, G. Gerdts, O. Wurl and B. M. Scholz-Böttcher, *Nat. Commun.*, 2023, **14**, 1–9.

12 Y. Y. Chen, X. T. Cheng and Y. Q. Zeng, *Int. J. Environ. Sci. Technol.*, 2023, **20**, 10477–10490.

13 I. Nesterovschi, I. Marica, E. A. Levei, S. B. Angyus, M. Kenesz, O. T. Moldovan and S. Cîntă Pînzaru, *Spectrochim. Acta, Part A*, 2023, **298**, 122811.

14 D. K. Gupta, D. Choudhary, A. Vishwakarma, M. Mudgal, A. K. Srivastava and A. Singh, *Int. J. Environ. Sci. Technol.*, 2022, **20**, 6865–6896.

15 I. V. Kirstein, A. Gomiero and J. Vollertsen, *Curr. Opin. Toxicol.*, 2021, **28**, 70–75.

16 V. K. Sharma, X. Ma, E. Lichtfouse and D. Robert, *Environ. Chem. Lett.*, 2023, **21**, 1933–1936.

17 B. E. Cunningham, E. E. Sharpe, S. M. Brander, W. G. Landis and S. L. Harper, *Front. Toxicol.*, 2023, **5**, 1154538.

18 J. Zhang, D. Fu, H. Feng, Y. Li, S. Zhang, C. Peng, Y. Wang, H. Sun and L. Wang, *TrAC, Trends Anal. Chem.*, 2024, **170**, 117472.

19 A. Käppler, D. Fischer, S. Oberbeckmann, G. Schernewski, M. Labrenz, K. J. Eichhorn and B. Voit, *Anal. Bioanal. Chem.*, 2016, **408**, 8377–8391.

20 M. Willans, E. Szczecinski, C. Roocke, S. Williams, S. Timalsina, J. Vongsvivut, J. McIlwain, G. Naderi, K. L. Linge and M. J. Hackett, *Environ. Sci.:Adv.*, 2023, **2**, 663–674.

21 C. F. Araujo, M. M. Nolasco, A. M. P. Ribeiro and P. J. A. Ribeiro-Claro, *Water Res.*, 2018, **142**, 426–440.

22 I. Marica, M. Aluaș and S. Cîntă Pînzaru, *Waste Manage.*, 2022, **144**, 479–489.

23 H. Cai, E. G. Xu, F. Du, R. Li, J. Liu and H. Shi, *Chem. Eng. J.*, 2021, **410**, 128208.

24 R. S. Das and Y. K. Agrawal, *Vib. Spectrosc.*, 2011, **57**, 163–176.

25 R. R. Jones, D. C. Hooper, L. Zhang, D. Wolverson and V. K. Valev, *Nanoscale Res. Lett.*, 2019, **14**, 1–34.

26 M. Moskovits, Surface-Enhanced Raman Scattering: Physics and Applications, in *Topics in Applied Physics*, ed. K. Kneipp, M. Moskovits and H. Kneipp, Springer, Berlin & Heidelberg, 2006, vol. 1, pp. 1–17.

27 R. Pilot, R. Signorini, C. Durante, L. Orian, M. Bhamidipati and L. Fabris, *Biosensors*, 2019, **9**, 57.

28 X. X. Han, R. S. Rodriguez, C. L. Haynes, Y. Ozaki and B. Zhao, *Nat. Rev. Methods Primers*, 2022, **1**, 1–17.

29 C. Farcau and S. Astilean, *J. Mol. Struct.*, 2014, **1073**, 102–111.

30 N. K. Mogha and D. Shin, *TrAC, Trends Anal. Chem.*, 2023, **158**, 116885.

31 L. Mikac, I. Rigó, L. Himics, A. Tolić, M. Ivanda and M. Veres, *Appl. Surf. Sci.*, 2023, **608**, 155239.

32 Y. Qin, J. Qiu, N. Tang, Y. Wu, W. Yao and Y. He, *Environ. Res.*, 2023, **228**, 115926.

33 R. Hu, K. Zhang, W. Wang, L. Wei and Y. Lai, *J. Hazard. Mater.*, 2022, **429**, 128388.

34 G. Li, Z. Yang, Z. Pei, Y. Li, R. Yang, Y. Liang, Q. Zhang and G. Jiang, *Talanta*, 2022, **249**, 123701.

35 X. X. Zhou, R. Liu, L. T. Hao and J. F. Liu, *Talanta*, 2021, **221**, 121552.

36 L. Lv, L. He, S. Jiang, J. Chen, C. Zhou, J. Qu, Y. Lu, P. Hong, S. Sun and C. Li, *Sci. Total Environ.*, 2020, **728**, 138449.

37 J. Caldwell, P. Taladriz-Blanco, L. Rodriguez-Lorenzo, B. Rothen-Rutishauser and A. Petri-Fink, *Environ. Sci.: Nano*, 2024, **11**, 1000–1011.

38 B. Chaisrikhwun, S. Ekgasit and P. Pienpinijtham, *J. Hazard. Mater.*, 2023, **442**, 130046.

39 J. Zhang, M. Peng, E. Lian, L. Xia, A. G. Asimakopoulos, S. Luo and L. Wang, *Environ. Sci. Technol.*, 2023, **57**, 8365–8372.

40 S. Luo, J. Zhang and J. C. de Mello, *Front. Bioeng. Biotechnol.*, 2023, **11**, 1242797.

41 Q. Yang, S. Zhang, J. Su, S. Li, X. Lv, J. Chen, Y. Lai and J. Zhan, *Environ. Sci. Technol.*, 2022, **56**, 10818–10828.

42 L. Chang, S. Jiang, J. Luo, J. Zhang, X. Liu, C. Y. Lee and W. Zhang, *Environ. Sci.: Nano*, 2022, **9**, 542–553.

43 G. Xu, H. Cheng, R. Jones, Y. Feng, K. Gong, K. Li, X. Fang, M. A. Tahir, V. K. Valev and L. Zhang, *Environ. Sci. Technol.*, 2020, **54**, 15594–15603.

44 M. J. Natan, *Faraday Discuss.*, 2006, **132**, 321–328.

45 H. W. Deckman and J. H. Dunsmuir, *Appl. Phys. Lett.*, 1982, **41**, 377–379.

46 C. Farcau, *Sci. Rep.*, 2019, **9**, 1–9.

47 R. P. Van Duyne, J. C. Hulteen and D. A. Treichel, *J. Chem. Phys.*, 1993, **99**, 2101–2115.

48 L. Ouyang, W. Ren, L. Zhu and J. Irudayaraj, *Rev. Anal. Chem.*, 2017, **36**, 20160027.

49 F. Xing, W. Duan, J. Tang, Y. Zhou, Z. Guo, H. Zhang, J. Xiong and M. Fan, *Anal. Chem.*, 2025, **97**, 2293–2299.

50 E. C. Le Ru, E. Blackie, M. Meyer and P. G. Etchegoint, *J. Phys. Chem. C*, 2007, **111**, 13794–13803.

51 C. M. Whelan, M. R. Smyth and C. J. Barnes, *Langmuir*, 1999, **15**, 116–126.

52 N. Nechita and C. Farcău, *Opt. Express*, 2021, **29**, 42238–42250.

53 X. Ye and L. Qi, *Nano Today*, 2011, **6**, 608–631.

54 T. H. Joo, M. S. Kim and K. Kim, *J. Raman Spectrosc.*, 1987, **18**, 57–60.

55 J. Zuloaga and P. Nordlander, *Nano Lett.*, 2011, **11**, 1280–1283.

56 D. Kurouski, N. Large, N. Chiang, A. I. Henry, T. Seideman, G. C. Schatz and R. P. Van Duyne, *J. Phys. Chem. C*, 2017, **121**, 14737–14744.

57 R. J. C. Brown and M. J. T. Milton, *J. Raman Spectrosc.*, 2008, **39**, 1313–1326.

58 A. Palm, *J. Phys. Colloid Chem.*, 1951, **55**, 1320–1324.

59 J. R. Anema, A. G. Brolo, A. Felten and C. Bittencourt, *J. Raman Spectrosc.*, 2010, **41**, 745–751.